Dielectric and piezoelectric properties of (K$_{0.475}$Na$_{0.495}$Li$_{0.03}$)NbO$_3$-0.003ZrO$_2$/PVDF 0–3 composite reinforced with two types of nano-ZnO particles

Kun Yu[1] · Shan Hu[1,2] · Junqin Tan[1] · Wendi Yu[1]

Abstract

(K$_{0.475}$Na$_{0.495}$Li$_{0.03}$) NbO$_3$–0.003ZrO$_2$ (KNNL-Z) ceramic was synthesized by the conventional solid-state reaction method. The purchased ZnO nanorods (denoted as ZnO1) and synthesized ZnO nanocakes (denoted as ZnO2) were used in the preparation of two types of composites fabricated by hot-pressing process using KNNL-Z ceramic powder, two kinds of ZnO nanoparticles, and PVDF polymer. The effects of the ZnO nanoparticles on the crystalline structures, morphology, thermal, dielectric, and piezoelectric properties of the composites were studied systemically. The KNNL-Z ceramic possesses a perovskite-type orthorhombic phase and the PVDF polymer mainly possesses α, β, and γ phases. Two kinds of ZnO all possess hexagonal wurtzite structures without any impurity phase. Interestingly, the incorporation of the ZnO nanoparticles has great impact on lattice constants and strain. In addition, the β phase content increases when the ZnO nanoparticles are added. From differential scanning calorimetry (DSC) measurements, it is found that the ZnO nanoparticles can enhance the thermal stability of composites. Moreover, the dielectric and piezoelectric properties are also found to be improved with the increase of ZnO content. Especially when 10 wt% ZnO2 is added, the dielectric constant reaches the value of 469.4 (100 Hz) at room temperature and the piezoelectric coefficient is 55 pC/N. After 30 days of aging test, it is obvious that all the composites present a good stability of piezoelectric property.

✉ Shan Hu
hushan@cug.edu.cn

Kun Yu
ujo7400673@163.com

Junqin Tan
1484646698@qq.com

Wendi Yu
771267404@qq.com

1   Faculty of Materials Science and Chemistry, China University of Geosciences, No. 388. Lumo Road, Hongshan District, Wuhan 430074, Hubei Province, People's Republic of China

2   Engineering Research Center of Nano, Geomaterials of Ministry of Education, China University of Geosciences, Wuhan 430074, People's Republic of China

1 Introduction

With the development of electronic science and technology, excellent piezoelectric and dielectric materials are increasingly needed in the field of electronic devices. Lead zirconate titanate (PZT)-based ceramics have been widely applied in piezoelectric devices in the past few decades due to their excellent piezoelectric properties [1]. However, due to their lead content, PZT ceramics have caused a series of environmental and health problems. PZT ceramics are being replaced by more and more lead-free ceramics. However, the traditional lead-free ceramics, such as BaTiO$_3$ (BT) and Na$_{1-x}$K$_x$NbO$_3$ (KNN) are not appropriate to satisfy the application requirements because these materials are stiff, brittle, and hard to be processed. Poor reliabilities have become critical limitation on the performance of the devices under severe circumstances. Whereas polymers, such as PVDF, poly (vinylidene fluoride-trifluoroethylene) [P(VDF-TrFE)], and poly (vinylidene fluoride-trifluoroethylene-chlorofluoroethylene) [P(VDF-TrFE-CFE)], possess outstanding flexibility and relatively low processing temperature [2]. Advanced structural and functional composites

are expected to be a good solution to these problems. Therefore, ceramic/polymer composites receive increasing attention due to it integration of the advantages of two component materials. The simplest ceramic/polymer composite is that which consists of ceramic particles randomly dispersed in polymer matrix, which is well known as 0–3 connectivity [3].

However, nowadays, ceramic/polymer 0–3 composites are scarce in electromechanical transducers, sensors, actuators, and other electronic devices because the piezoelectric and dielectric constants of ceramic/polymer 0–3 composites are much lower than those of ceramics. Therefore, the key material with high piezoelectric and dielectric constant, low loss tangent, and easy processing characteristics becomes more and more imperative. To increase the electrical properties, different approaches were examined. One approach is to increase the dielectric constant of the polymer matrix. For example, the chemical pinning of P(VDF-TrFE) results in the relaxor ferroelectric (RFE) behavior by using electron beam [4]. A dielectric constant higher than 100 was obtained in an irradiated P(VDF-TrFE). Another approach is to use the Maxwell–Wagner–Silar (MWS) effect. The enhancement of electrical properties of composites were obtained by using $CaCu_3Ti_4O_{12}$ (CCTO), multi-walled carbon nanotubes (MWCNT), Mn, Ni, or ZnO, and so on in recent years [5–9]. Interesting, in PVDF/ZnO composite, many researchers have found that ZnO can enhance the content of β phase in PVDF and greatly improve its dielectric and piezoelectric properties. In addition, the ZnO also can prevent the particles aggregation and influence the thermal stability [10–13].

In this work, two types of novel ceramic–polymer–filler ternary composite systems were prepared using $0.997(K_{0.475}Na_{0.495}Li_{0.03})$ NbO_3–$0.003ZrO_2$ ceramic, PVDF as polymer matrix, and two kinds of ZnO as the filler. These composites were fabricated via a simple blending and hot-molding technique. Then, the structure and thermal stability were studied in detail, and, also, the electrical properties were investigated systemically.

2 Experimental procedure

2.1 Preparation of KNNL-Z ceramic powder

$0.997(K_{0.475}Na_{0.495}Li_{0.03})$–$0.003ZrO_2$ ceramic powder was prepared by a conventional solid-state reaction. The raw materials were K_2CO_3 (Aldrich 99.99%), Na_2CO_3 (Aldrich 99.8%), Li_2O_3 (Aldrich 99%), Nb_2O_5 (Aldrich 99.9%), and ZrO_2 (Aldrich 99%). These materials were dried at 60 °C for 24 h to remove any moisture, and weighted according to their stoichiometric formulas. Then, the materials were ball-milled for 24 h in ethanol with zirconia balls to obtain a homogenous mixture. The mixture was dried and calcined at 850 °C for 3 h in a covered alumina crucible. After calcination, the powder was crushed and ball-milled again for 24 h. After drying, the powder was mixed with 5 wt% polyvinyl alcohol (PVA) as binder and pressed into disks 14 mm in diameter and about 1 mm in thickness at 10 MPa. The disks were buried in alumina powder and heated at 650 °C for 5 h to remove the PVA component. Subsequently, the disks were sintered in the temperature at 1080–1120 °C for 3 h in ambient atmosphere and crushed into powder by high-speed mill.

2.2 Preparation of ZnO powder

Two types of ZnO were used in this work. The first kind of ZnO (ZnO1) was supplied by Sinopharm Chemical Reagent Co., China. The second kind of ZnO (ZnO2) was grown by hydrothermal method. For the synthesis of ZnO2 nanoparticles, in the first step, 1.756 g of Zn $(CH_3COO)_2·2H_2O$ and 2.956 g of CTAB were dissolved in 40 mL of deionized water. The zinc precursor solution was kept in constant stirring for 30 min. In the second step, 0.32 g of NaOH was dissolved in 40 mL of deionized water and then mixed with the zinc precursor solution drop by drop, keeping the solution at constant stirring for 30 min. Then, the solution was transferred into polytetrafluoroethylene autoclave which was kept inside an oven at 140 °C for 12 h. After cooling to room temperature, the solution was centrifuged at 3000 rpm and washed with absolute ethyl alcohol. The ZnO2 nanoparticles were filtered and kept to dry in an oven maintained at 60 °C for 12 h.

2.3 Preparation of KNNL-Z/PVDF/ZnO ternary composites

PVDF was provided by Shanghai 3F Co.,China. According to our previous study [14], the combination ratio of KNNL-Z/PVDF composite is the best when the ceramic content is 80 wt% (abbreviate as KNNL-Z/PVDF). Therefore, the weight ratio between KNNL-Z ceramic and PVDF polymer is 8:2 in all samples. Different weight percentages (2, 4, 6, 8, and 10 wt%) of ZnO powder were mixed in KNNL-Z ceramic and PVDF powder by using absolute ethyl alcohol. The mixture was continuously stirred by using a magnetic stirrer for 30 min at 500 rpm at 80 °C and evenly ultrasonically dispersed at 60 °C for 30 min. The mixture was dried at 60 °C for 24 h. The dried powder was then pressed into disks 14 mm in diameter and about 1 mm in thickness at 10 MPa. After that, the disks were heated by hot pressing at 200–220 °C for 10 min and polished.

2.4 Characterization

The structural properties and phases compositions of the KNNL-Z powder, pure PVDF and KNNL-Z/PVDF

composite, and KNNL-Z/PVDF/ZnO composite samples were determined by using a Bruker AXS D8-Focus (Germany) with *Cu Kα* radiation. The FTIR spectra of the samples were performed by using a Thermo Nicolet Corporation NEXUS 670 (USA). The fractured surface micro-structural images were carried out at room temperature by using a scanning electron microscope (SEM) Hitachi SU-8010 (Japan). The bulk densities were measured by a high-precision electronic gravity meter DahoMeter DE-200 M (China) using the Archimedes' principle. The differential scanning calorimeter (DSC) (NETZSCH STA 409 PC/PG) (Germany) was used to measure the thermal stability of composites. The samples were heated up from room temperature to 250 °C with the rate of 10 °C/min on Al_2O_3 pan under a N_2 ambient. In order to measure the electrical properties, the samples were coated with silver paste electrodes. The electric poling of samples was carried out at 100 °C in a silicone oil bath by applying a DC field of 3–6 kV/mm for 30 min. The samples were placed in the air atmosphere for 24 h. Then, the dielectric constant ε_r was determined by using a Keysight Technologies E4990A (USA) device. The piezoelectric coefficient d_{33} was measured by using a Piezotest PM-200 (UK) set up at 110 Hz. The piezoelectric coefficients of samples were tested several times within 30 days in order to investigate the piezoelectric stability.

3 Results and discussion

3.1 X-ray structural studies

The XRD patterns of PVDF polymer, KNNL-Z ceramic, and KNNL-Z/PVDF 0–3 composite are shown in Fig. 1a. The XRD pattern of PVDF polymer presents the presence of a semicrystalline mixture composed of α, β, and γ phases. The characteristic peaks of α phase are corresponding to $2\theta = 17.4°$ (100) and 18.5° (022). The characteristic peak of β phase in 2θ is corresponding to 20.1° (110). The characteristic peaks at $2\theta = 26.5°$ (022) and 38.6° (211) are corresponding to γ phase [15, 16]. The KNNL-Z ceramic possesses a pure perovskite phases without any impurity phase. Comparing the intensities of peaks between 45.2° (002) and 46.1° (200), the phase of ceramic is orthorhombic symmetry [17]. The XRD patterns of all composite mainly reveal the phases of KNNL-Z ceramic and ZnO, but the peak intensities are weakened. The XRD patterns of ZnO1, ZnO2, and the composites doped with different weight fractions of ZnO1 or ZnO2 are shown in Fig. 1b and c. The two kinds of ZnO possess hexagonal wurtzite structures without any other secondary phase. The cell parameters of hexagonal wurtzite structure are evaluated based on the data for (100) and (002) planes.

Fig. 1 a The XRD patterns of PVDF polymer, KNNL-Z/PVDF composite, and KNNL-Z ceramic. **b** The XRD patterns of pure ZnO1 and KNNL-Z/PVDF/ZnO1 composites. **c** The XRD patterns of pure ZnO2 and KNNL-Z/PVDF/ZnO2 composites
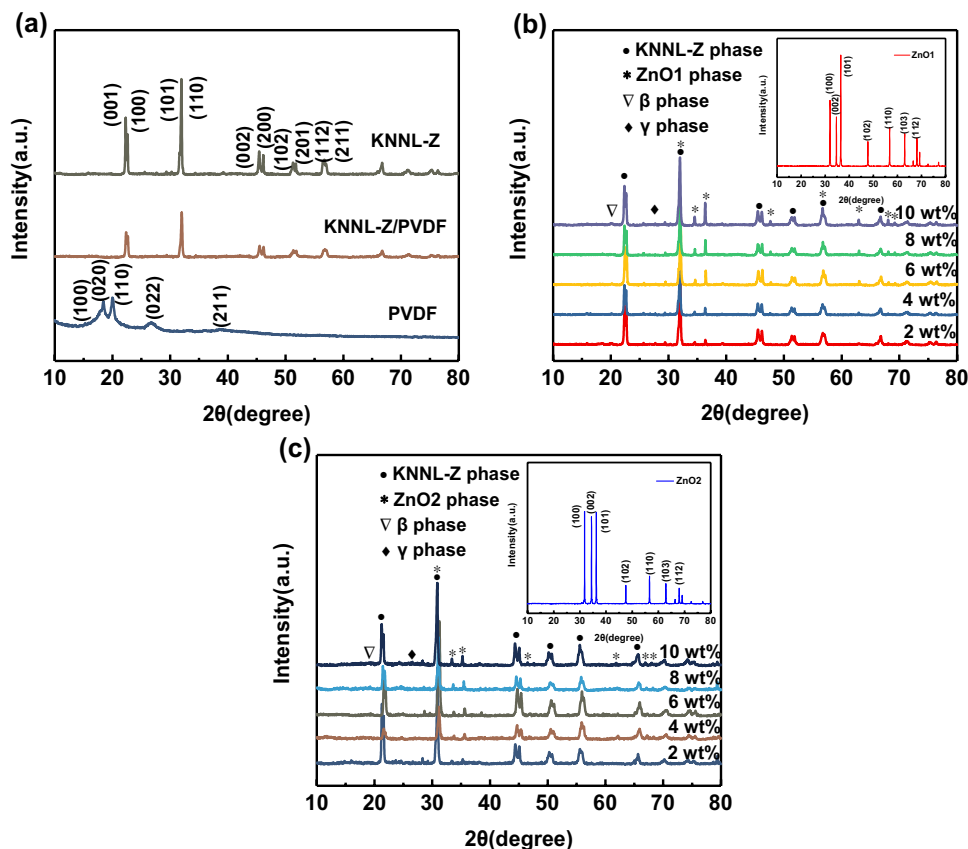
For the (100) plane, the cell parameter a is calculated by Eq. (1):

$$a = \frac{\lambda}{\sqrt{3}\sin\theta},\qquad(1)$$

where $\lambda = 0.1542$ nm is the wavelength of $Cu\ K\alpha$ source and θ is the Bragg's diffraction angle.

For the (002) plane, the cell parameter c is calculated by Eq. (2):

$$c = \frac{\lambda}{\sin\theta}\qquad(2)$$

In addition, the lattice strain of ZnO is calculated by Eq. (3):

$$\varepsilon = \frac{\beta_{FWHM}\cos\theta}{4},\qquad(3)$$

where β_{FWHM} is the full width at half maximum (FWHM) of diffraction peak. The cell parameters and strains of ZnO are shown in Table 1. It is observed that, when ZnO nanoparticles are added in composites, the cell parameters and strains increase with the increase of ZnO content. This phenomenon demonstrates that the doped element Zn^{2+} can occupy the A-site or B-site of ABO_3 type of perovskite structure and thus effect the crystal structure. Comparing the ionic radii of Zr^{4+} (0.72 Å) with Nb^{5+} (0.64 Å) at the coordination number is 6, Zr^{4+} can occupy the B-site and generate the oxygen vacancies and A-site vacancies [18]. However, in view of the ionic radius of Zn^{2+} (0.74 Å) being closer to that of Zr^{4+} or Nb^{5+} as compared to those of Na^+ (1.49 Å), K^+ (1.64 Å), Li^+ (1.76 Å). It may be due to that the possibility of diffusing Zn^{2+} into B-site to partially replace Zr^{4+} and Nb^{5+} ions is more than that of its diffusion into A-site. When Zn^{2+} is substituted into Zr^{4+} or Nb^{5+} sites within the perovskite ABO_3 structure, it will generate lattice strain and oxygen vacancies.

$$ZnO \rightarrow Zn''_{Zr\ or\ Nb} + V_O^{\bullet\bullet} + O_o^{\times}\qquad(4)$$
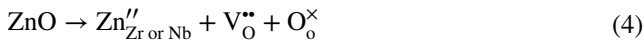
Charged oxygen vacancies, in combination with Zn ions, obviously give rise to local deformation within perovskite unit cells and thus increasing the lattice parameter [19, 20]. This result is also in agreement with the previous research reported by Parangusan, H [21]. According to the research of Zhang, the lattice strains increased by dopants enhanced the piezoelectric properties of ZnO [22]. This theory is subsequently confirmed by the piezoelectric test of samples.

The average crystallite size can be calculated by the Scherer formula:

$$\text{Crystallite size} D = \frac{0.9\lambda}{\beta_{FWHM}\cos\theta}\qquad(5)$$

Table 1 The lattice constants a, c, and strain of pure ZnO1, pure ZnO2, ZnO1, and ZnO2 in composites

Sample	ZnO1	KNNL-Z/PVDF/ZnO1					ZnO2	KNN-Z/PVDF/ZnO2				
ZnO (wt%)	100	2	4	6	8	10	100	2	4	6	8	10
a (Å)	3.2282	4.0709	4.2249	4.2297	4.2843	4.2963	3.3125	4.2107	4.2671	4.2730	4.2767	5.850
c (Å)	5.1541	3.1310	4.1043	4.1088	4.1586	5.2217	5.7523	3.9275	4.1323	4.2909	4.8297	4.9297
Strain (%)	0.051±0.0035	0.285±0.0090	0.300±0.0124	0.355±0.0150	0.363±0.0203	0.404±0.0130	0.065±0.0142	0.359±0.0207	0.380±0.0178	0.402±0.0155	0.414±0.0167	0.447±0.0224

If the crystallite size of the substance is larger than 100 nm, the stress-induced broadening is remarkable. In this case, such broadening must be considered, the Scherer formula is not applicable. If the crystallite size is less than 100 nm, the crystallite size of the substance in this paper was obviously less than 100 nm, the stress-induced broadening is negligible compared to the broadening caused by the crystallite size [23]. The calculated crystallite sizes of pure ZnO1 and ZnO2 are 16.2 and 11.8 nm, respectively. The crystallite sizes of ceramic are given in Online Resource 1. The crystallite sizes of ceramic in composites are found to enhance with the increase of ZnO content. According to Atuchin V.'s research, the concentration of the dopant affects the cell constant of the crystal and it has been found that this variation is a transition from a full oxygen sublattice to a sublattice with vacancies [24]. The real reason for the change of cell parameters in this paper is not clear. We think the possible reasons for the crystallite size growth are as follows: Zn^{2+} enters into B-site of the perovskite structure to substitute for Zr^{4+} or Nb^{5+} and oxygen vacancies are created. This is assumed to be responsible for the promoted crystallite size growth as the content of ZnO increases [25].

3.2 Fourier transform infrared (FTIR) analysis

In Fig. 2a, the FTIR spectra are shown for the pure PVDF polymer, KNNL-Z/PVDF composite, and KNNL-Z/PVDF/ZnO composites in the wave number range of 600–2000 cm^{-1}. The peaks at 614, 764, 796, and 976 cm^{-1} correspond to the α phase in PVDF polymer [26, 27]. The bands at 840, 875, 1070, 1276, and 1401 cm^{-1} are considered to be characteristics of the β phase in PVDF polymer [28, 29]. The peaks identified the γ phase are 840 and 834 cm^{-1} [30]. It can be seen that the characteristic absorption peaks of α, β, and γ phases appear in all samples. However, the band at 840 cm^{-1} is observed for both β and γ phases. In order to separate out the β and γ phases, the FTIR spectra with the transmission (y-axis) are transformed into the FTIR spectra with the absorbance as y-axis, and the deconvolutions of the FTIR spectra are shown in Fig. 2c. To quantify the variation of the β phase with the increase in ZnO loading, the fraction of the β phase content $F(\beta)$ was calculated by using the Beer–Lambert law:

$$F(\beta) = \frac{A_\beta}{(K_\beta/K_\alpha)A_\alpha + A_\beta}, \tag{5}$$

where $K_\alpha = 6.1 \times 10^4$ cm^2/mol and $K_\beta = 7.7 \times 10^4$ cm^2/mol are the absorption coefficients at 764 and 840 cm^{-1}, A_α and A_β are the absorbance levels at 764 and 840 cm^{-1}, respectively.

The calculated values of $F(\beta)$ are represented in Fig. 2b. It is observed that the content of the β phase increases with the addition of ZnO. PVDF polymer is made up of repeating units (CH_2–CF_2 monomer). Different phases in PVDF polymer can be produced when hydrogen and fluorine atoms are arranged in different way. When ZnO is added to the composites, the negative surface charges in ZnO interact with CH_2 dipoles and the positive surface charges in ZnO interact with CF_2 dipoles. This can lead to the formation of all-trans conformation (Namely: TTTT chains, which correspond to the β phase) [31, 32]. It indicates that the interaction between polymer chains and ZnO may result in the β phase growth. In addition, it is worth noting that $F(\beta)$ of KNNL-Z/PVDF/ZnO2 composites is higher than that of KNNL-Z/PVDF/ZnO1 composites at higher contents of ZnO. Therefore, the piezoelectric properties of the composites doped with ZnO may be enhanced and the piezoelectric properties of KNNL-Z/PVDF/ZnO2 composites may be higher than those of KNNL-Z/PVDF/ZnO1 composites.

3.3 Micro-structural characterization

The SEM images of two types of ZnO nanoparticles, KNNL-Z/PVDF composite (The SEM image of KNNL-Z/PVDF composite is given in Online Resource 2) and KNNL-Z/PVDF/ZnO composites are shown in Fig. 3a and b. From Fig. 3a2–a6, b2–b6, and the energy-dispersive X-ray spectroscopy (EDS) images of all samples (The EDS images of all samples are given in Online Resource 3), it is seen that the KNNL-Z ceramic and ZnO1 nanoparticles can be well dispersed in PVDF polymer, but the formation of small pores at 6 wt% ZnO1 content in KNNL-Z/PVDF/ZnO1 composites is observed (Fig. 3a4). This may be attributed to hot-pressing process. The KNNL-Z ceramic and ZnO2 nanoparticles can be well dispersed in PVDF polymer, and KNNL-Z/PVDF/ZnO2 composites has few pores at all ZnO2 contents. It is clearly seen that the ZnO1 particle has irregular shape. Interestingly, the morphology of ZnO2 nanoparticle consisted of multiple ZnO nanorods which possess hexagonal prism shapes and stack along the c-axis. Its structure resembles a layered cake. The ZnO2 particles are well faceted. The faceted microcrystal shapes is a robust indicator of high crystal quality, as it was verified for many compounds from different chemical classes [33, 34].
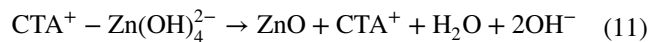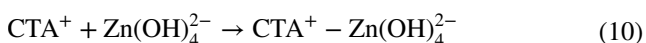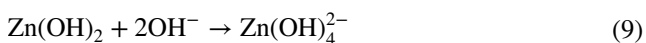
In order to understand the growth mechanism of the nano-cake structure comprehensively, the possible chemical reactions under the hydrothermal conditions are presented as follows:

$$Zn(CH_3COO)_2 + 4H_2O \rightarrow Zn(OH)_4^{2-} + 2CH_3COOH + 2H^+ \tag{6}$$

$$Zn^{2+} + 2OH^- \rightarrow Zn(OH)_2 \tag{7}$$
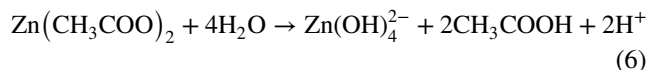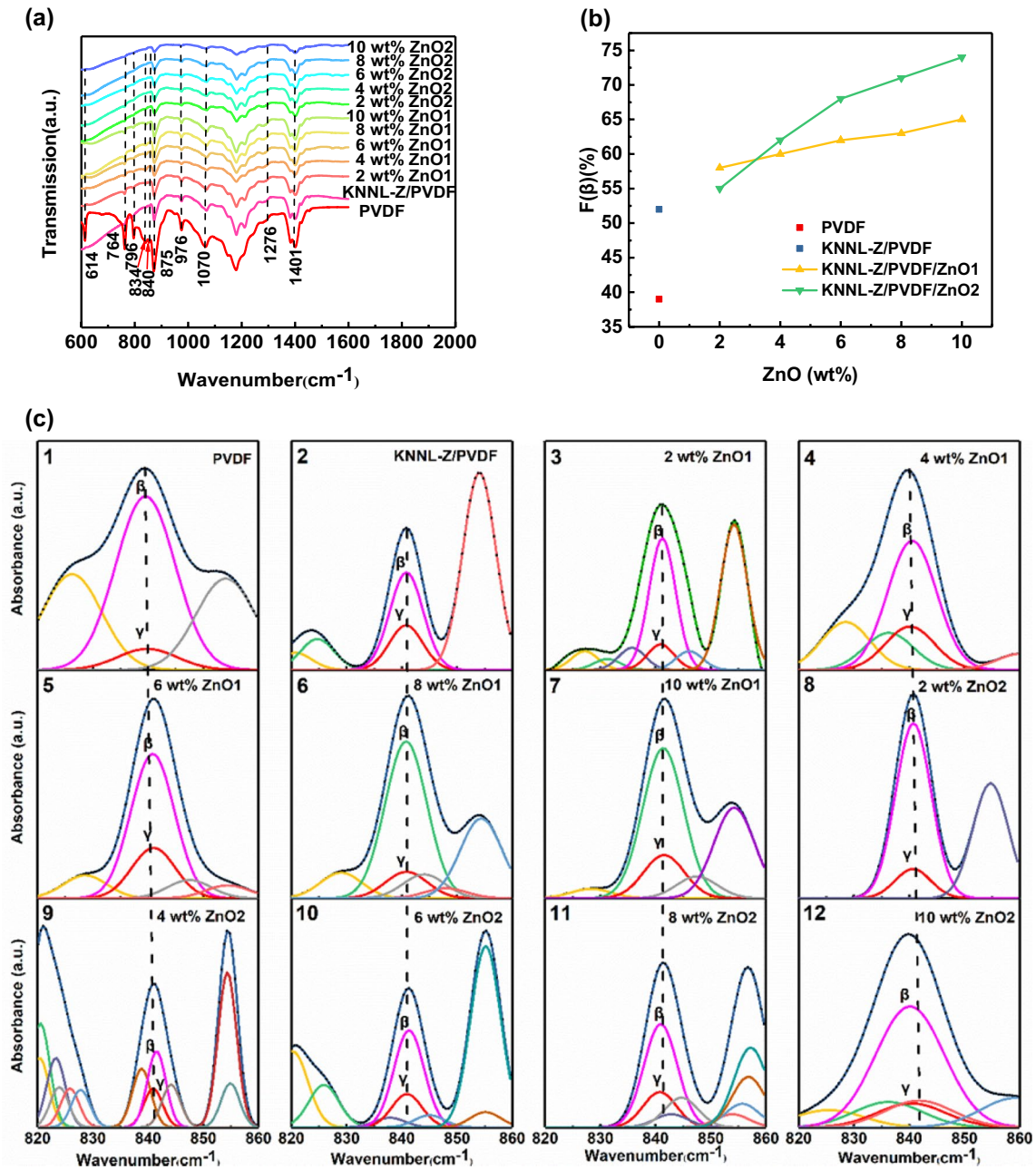
Fig. 2 **a** FTIR spectra of pure PVDF, KNNL-Z/PVDF composite, and KNNL-Z/PVDF/ZnO composites. **b** The ratios of the β phase in pure PVDF, KNNL-Z/PVDF, and KNNL-Z/PVDF/ZnO composites. **c** The deconvolutions of FTIR data of (1) pure PVDF, (2) KNNL-Z/PVDF composite. (3–7) KNNL-Z/PVDF/ZnO1 composites and (8–12) KNNL-Z/PVDF/ZnO2 composites

$$CTAB \rightarrow CTA^+ + Br^- \tag{8}$$

$$Zn(OH)_2 + 2OH^- \rightarrow Zn(OH)_4^{2-} \tag{9}$$

$$CTA^+ + Zn(OH)_4^{2-} \rightarrow CTA^+ - Zn(OH)_4^{2-} \tag{10}$$

$$CTA^+ - Zn(OH)_4^{2-} \rightarrow ZnO + CTA^+ + H_2O + 2OH^- \tag{11}$$

On the basis of the SEM observation and analysis, the evolution process of the ZnO nanocakes is proposed and the growth mechanism of ZnO nanocakes is shown in Fig. 3c. CTAB is a kind of cationic surfactant, which can reduce the surface tension of the solution and increase the dispersion of ZnO nanoparticles [35]. In addition, the positively charged CTA^+ has a hydrophilic head
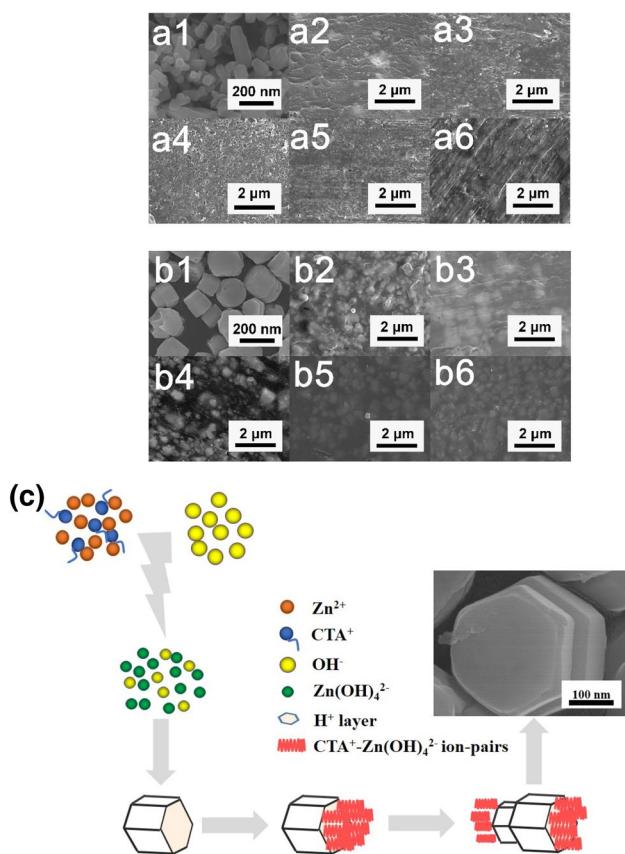
Fig. 3 SEM micrographs of the fractured surfaces of ZnO1 (**a1**), ZnO2 (**b1**), and KNNL-Z/PVDF/ZnO composites with ZnO content of (**a2** and **b2**) 2 wt%, (**a3** and **b3**) 4 wt%, (**a4** and **b4**) 6 wt%, (**a5** and **b5**) 8 wt%, (**a6** and **b6**) 10 wt%. **c** The growth mechanism of ZnO nanocake (ZnO2)

and a hydrophobic tail clings to the negatively charged $Zn(OH)_4^{2-}$ nuclei to form the $CTA^+ - Zn(OH)_4^{2-}$ negatively charged ion pairs due to electrostatic interaction [36]. The $CTA^+ - Zn(OH)_4^{2-}$ negatively charged ion pairs can adhere to the positively charged (001) surface of ZnO. At the same time, the hydrophobic tails of CTA^+ form a film. The hydrophobic film inhibits the growth of (001) and led to formation of hexagonal low aspect ratio ZnO crystals [37]. On the other hand, there are certain amount of positively charged H^+ ions in the reaction system. The negative charged $(00\bar{1})$ surface can absorb these H^+ ions and form the H^+ layer. Whereafter, the H + layer can absorb the negatively charged $CTA^+ - Zn(OH)_4^{2-}$ ion pairs and enhance the growth along this direction. Therefore, a bud grows out on each end of the formed ZnO prisms on their $(00\bar{1})$ surface. The ZnO prisms grow larger and larger as time goes on and form the ZnO nanocake structure finally.

3.4 Thermal properties

Thermal stability of the polymer composites is critical for practical applications and the existence of fillers may change thermal characteristics of resulting composites. The crystallization behavior of pure PVDF and PVDF in composites were studied using DSC in this study. The dynamic DSC curves of the pure PVDF and all composites in the temperature range of 120–200 °C at heating rate of 10 °C/min were obtained, as shown in Fig. 4. It can be seen in Fig. 4a that the crystallization peak temperatures T_c of PVDF and KNNL-Z/PVDF composites are very close. Of interest is that, as shown in Fig. 4b and c, the crystallization peak temperatures of KNNL-Z/PVDF/ZnO composites shift to higher temperatures and the crystallization peak temperatures increase gradually with the increase of ZnO addition. This phenomenon is the same as what other researchers have found [38, 39]. The enhancement of crystallization peak temperature of the KNNL-Z/PVDF/ZnO composites may be ascribed to the following factors: (1) The mobility of polymer chains can decrease when the polymer chains combine with ZnO particles, which is due to the battier effect of ZnO. ZnO acts as a mass transport barrier between the polymer chains [40]. This phenomenon occurs when the polymer chains are bound with the ZnO superstructure. (2) The ZnO nanoparticles inhibit the formation and escape of volatile by-products during degradation and the interactions between ZnO nanoparticles and PVDF polymer. It originates from the existence of hydrogen bonding between the PVDF polymer and the hydroxide groups on the ZnO surfaces [41]. (3) The incorporation of ZnO as an effective nucleation agent. When the ZnO is added to PVDF polymer, the ZnO nanoparticles induce a growth of crystalline layer around their surfaces and generate amounts of nucleation sites [42]. Therefore, the composites incorporated moderate amounts of ZnO can improve the thermal stability. The crystallinity X_c is shown in Fig. 4d. In spite of the interaction with the PVDF matrix, two kinds of ZnO nanoparticles up to 10 wt% have only slight effect on the crystallinity of PVDF. However, some researchers reported that the crystallinity of PVDF strongly decreases with increasing the content of different kinds of dopant like Au or Fe_3O_4 [43, 44]. It is worth noting that the crystalline phase controls the piezoelectricity of PVDF. Hence, crystallinities maintain basically the same values after ZnO incorporation and our composites doped with ZnO are expected to have high piezoelectric properties.

3.5 Density

Density is a significant physical property of 0–3 composite material. The experimental density of all KNNL-Z/PVDF/ZnO composites was obtained by the Archimedes' principle. The theoretical density of material is related to the volume

Fig. 4 The dynamic DSC curves of **a** pure PVDF polymer, **a** KNNL-Z/PVDF composite, **b** KNNL-Z/PVDF/ZnO1 composites, and **c** KNNL-Z/PVDF/ZnO2 composites. **d** The crystallinities X_c of all samples
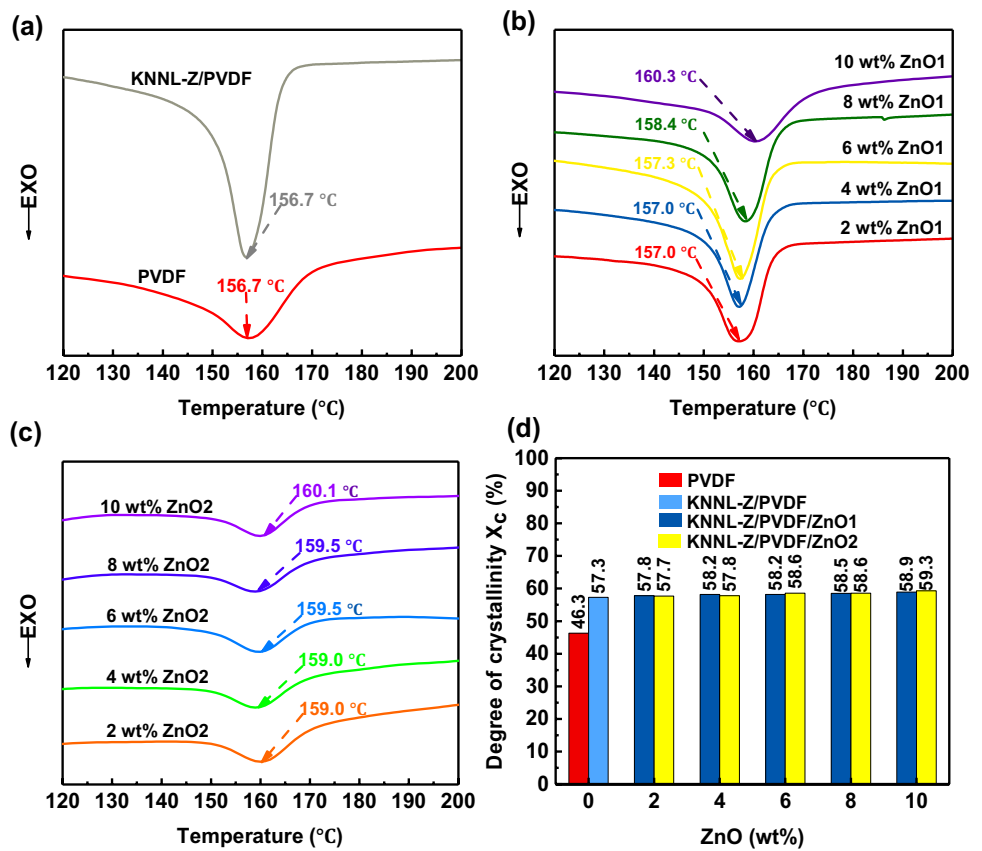

fraction and the density of each component and it can be estimated by using following equation:

$$\rho = \emptyset_c \rho_c + \emptyset_z \rho_z + \left(1 - \emptyset_c - \emptyset_z\right)\rho_m, \quad (11)$$

where ρ is the theoretical density of composite, ρ_c, ρ_z, and ρ_m are the densities of the KNNL-Z ceramic (3.9605 g/cm³), ZnO (5.606 g/cm³), and PVDF (1.750 g/cm³), respectively, $\emptyset_c$ and $\emptyset_z$ are the volume fractions of the KNNL-Z ceramic and ZnO, respectively. The experimental and theoretical densities and poriness of all composites are shown

in Fig. 5a. It is obvious that with the increase of the ZnO content, both the two kinds of density always lower than theoretical density, but they gradually increase and get closer to the theoretical density. The experimental density increased from 84.2 to 93.5% of the theoretical density. This phenomenon can be attributed to the existence of some gaps and pores between the KNNL-Z ceramic particles, ZnO, and the PVDF polymer. It is interesting to note that the defects decrease with increasing of ZnO content, it is also can be verified in Fig. 5b. In our previous study, it was found that the increase in KNNL-Z ceramic content would lead to a

Fig. 5 **a** Variation of the densities with ZnO content in the composites. **b** The porosity of all composites with different ZnO weight fractions
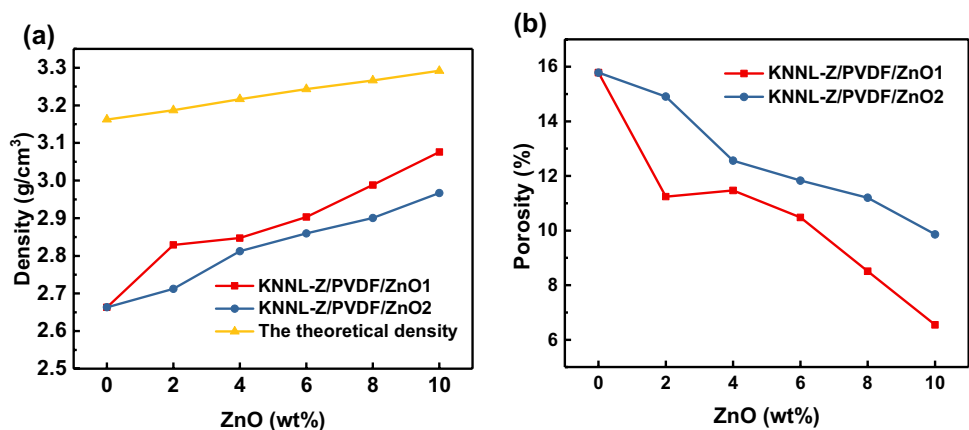
gradual increase in porosity in the composite [14]. Nevertheless, in this work, ZnO was considered to be able to reduce the pores in composite. It may be because ZnO can improve the crystallinity of PVDF (as the above thermal analysis), making it easy for molecules in PVDF to get close to each other and crystallize. Molecules are arranged in a standard and orderly manner. The higher the degree of order, the higher the density would be. On the other hand, during the cooling process after hot pressing, ZnO also inhibits the formation and escape of volatile by-products in PVDF, thus reducing the formation of defects.

3.6 Dielectric properties

The dielectric constant (ε_r) and loss tangent ($tan\delta$) of pure KNNL-Z ceramic (a), KNNL-Z/PVDF composite (b), KNNL-Z/PVDF/ZnO1 composites (c), and KNNL-Z/PVDF/ZnO2 composites (d) as a function of frequency range from 10^2 to 10^7 Hz at room temperature are shown in Fig. 6.

Dielectric constant represents the ability to store a charge when the material is subjected to an electric field and reflects the dielectric properties. The dielectric constants of all samples show the same tendency and decrease with increase of frequency. This phenomenon is also reported in other studies [45, 46]. The dielectric constant usually keeps a high value at lower frequencies due to electron and ionic displacement polarization, relaxation polarization, dipolar polarization, and space charge polarization [46, 47]. Among all polarizations, the space charge polarization is the primary component [48]. When the frequency increases continuously, relaxation polarization, space charge polarization cannot respond to the applied electric field fast enough that lead to the decrease of dielectric constant. Moreover, ionic displacement polarization becomes weaker at higher frequencies. The dipoles play an important role in the electron and dipolar polarizations at higher frequencies [49]. At the same time, the remaining polarizations begin to lag behind the field, the dielectric constant presents lower value as frequency increases [50].

On the other hand, as expected, it can also be observed that the dielectric constants of KNNL-Z/PVDF/ZnO composites are higher than that of KNNL-Z/PVDF composite, as seen in Fig. 6b, c, and d. For example, at 100 Hz, the dielectric constants of all composites are shown in Table 2. The composite with 10 wt% ZnO2 nanocake has a dielectric constant of 469.4, which is 1.6 times of the dielectric constant of KNNL-Z/PVDF composite. The enhancement of dielectric constant of the composites doped with ZnO may be ascribed to the following reasons: (1) The entrapment of free charges between the insulator/conductor interfaces for heterogeneous system due to the Maxwell–Wagner–Silar effect [51]. When the current flows across the interfaces of two materials with different electrical conductivity, the interaction of ZnO nanoparticles

with polymer chains and the charges accumulation at the interfaces between the ZnO nanoparticles and PVDF chains are schematically depicted in Fig. 6g. This interfacial polarization increases with the amount of ZnO and it results in higher dielectric constant at higher ZnO contents. (2) A larger aspect ratio and higher surface area of a polarizable material lead to a greater dielectric constant [52, 53]. ZnO1 has a larger aspect ratio than ZnO2, however, ZnO2 has a higher surface area than ZnO1. Therefore, the dielectric constants have little difference between two kinds of KNNL-Z/PVDF/ZnO composites. (3) As mentioned above (FTIR analysis), ZnO can increase the content of the β phase, and the β phase also contributes to increase the dielectric constant [9].

In order to estimate the frequency stability in each sample, the following equation has been used to calculate it [54]:

$$S = \frac{\varepsilon_r(f = 100Hz) - \varepsilon_r(f = 1MHz)}{\varepsilon_r(f = 100Hz)} \times 100\% \qquad (12)$$

The results are shown in Table 2. It is observed that the S values of KNNL-Z/PVDF/ZnO composites are lower than that of KNNL-Z/PVDF composite. It indicates that the frequency stability of the composites can be enhanced by doping ZnO.

Furthermore, it can be seen clearly that loss tangent presents a higher value at the lower frequencies and has a general trend of decreasing with increment of frequency due to an accumulation of free charges at lower frequencies and attenuation of various polarizations at higher frequencies, indicating the relaxation process [55]. It is well known that loss tangent includes two kinds of losses, polarization loss and leakage loss. Therefore, the loss tangent can be expressed by Eq. (13):

$$\tan \delta = \tan \delta_p + \tan \delta_l, \qquad (13)$$

where $tan\delta_p$ is the polarization loss, which is mainly due to the above polarizations, and $tan\delta_l$ is the leakage loss, which is due to leakage current. According to Kramers–Krönig equation, the polarization loss can be expressed as in Eq. (14):

$$\tan \delta_p = \frac{(\varepsilon_s - \varepsilon_\infty)w\tau}{\varepsilon_s + \varepsilon_\infty w^2\tau^2}, \qquad (14)$$

where ε_s is static dielectric permittivity, ε_∞ is dielectric permittivity at optical frequencies, w is angular frequency, and τ is relaxation time. The leakage loss is the ratio of active current density to reactive current density and the value can be calculated by Eq. (15):

$$\tan \delta_l = \frac{\gamma}{w\varepsilon_0\varepsilon'_r}, \qquad (15)$$

where γ is the conductivity of the medium, ε'_r is the real part of the dielectric permittivity, and ε_0 is permittivity of
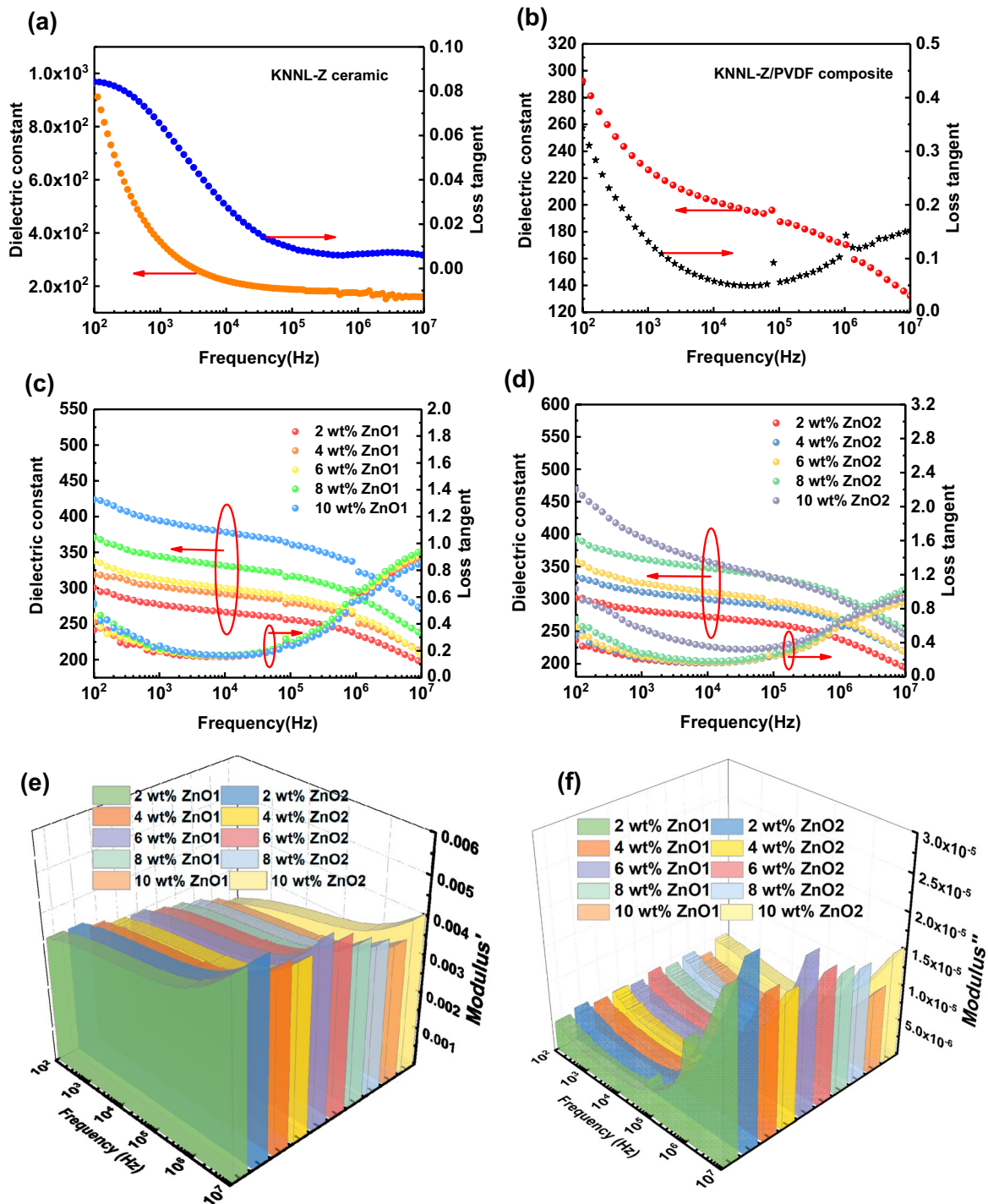
Fig. 6 Frequency dependence of dielectric constants and loss tangents of **a** KNNL-Z ceramic **b** KNNL-Z/PVDF composite, **c** KNNL-Z/PVDF/ZnO1 composites, and **d** KNNL-Z/PVDF/ZnO2 composites with different weight fractions. Frequency dependence of the **e** real and the **f** imaginary components of the electric modulus of com-posites with different weight fractions. **g** The charges accumulation of charge carriers in the interfaces between ZnO nanoparticles and PVDF chains. **h** Variation of the conductivity with ZnO content in the composites
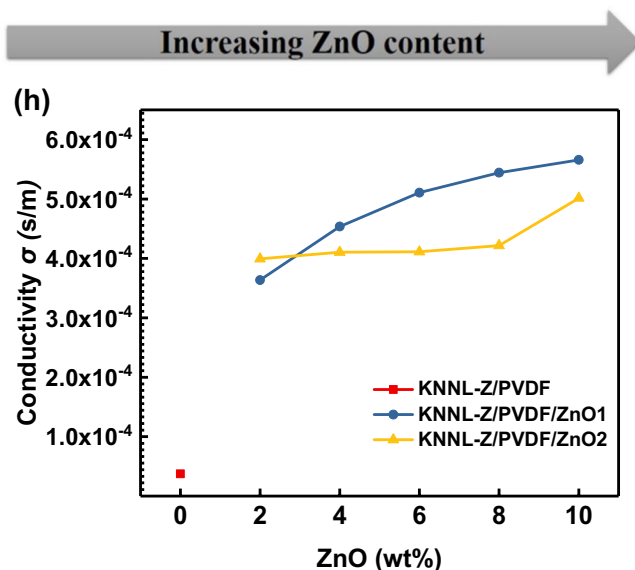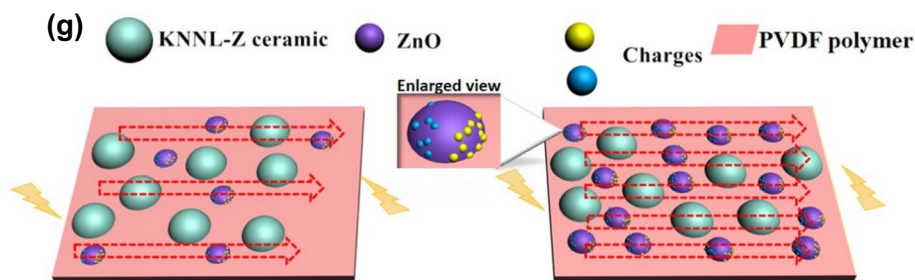
(g)

(h)

Fig. 6 (continued)

Table 2 The dielectric constants ε_r (100 Hz and 1 MHz) and the S values of all composites

Sample	KNNL-Z/PVDF	KNNL-Z/PVDF/ZnO1					KNNL-Z/PVDF/ZnO2				
ZnO (wt%)	0	2	4	6	8	10	2	4	6	8	10
ε_r (100 Hz)	292.4	300.7	318.8	338.2	370.8	424.1	301.3	334.2	357.8	391.8	469.4
ε_r (1 MHz)	170.3	233.5	250.6	258.7	285.4	322.7	236.7	261.6	266.2	300.1	296.6
S (%)	41.8	22.3	21.4	23.5	23.0	23.9	21.4	21.7	25.6	23.4	36.8

vacuum. Therefore, the loss tangent can be expressed by Eq. (16):

$$\tan\delta = \frac{(\varepsilon_s - \varepsilon_\infty)w\tau}{\varepsilon_s + \varepsilon_\infty w^2\tau^2} + \frac{\gamma}{w\varepsilon_0\varepsilon_r'} \quad (16)$$

$$\tan\delta \approx \frac{\gamma}{w\varepsilon_0\varepsilon_r'} \propto \frac{1}{w} \quad (17)$$

$$\tan\delta \approx \frac{(\varepsilon_s - \varepsilon_\infty)w\tau}{\varepsilon_s + \varepsilon_\infty w^2\tau^2} \propto \frac{1}{w} \quad (18)$$

When the angular frequency w of the electric field is close to 0 or $w\tau \leq 1$ at lower frequencies, the polarization loss $\tan\delta_p$ is close to 0 and only the leakage loss $\tan\delta_l$ can exist, the loss tangent tends to infinity, as in Eq. (17). When $w\tau \geq 1$ at higher frequencies, polarization loss becomes the main factor causing loss tangent. As shown in Eq. (18), the loss tangent is inversely proportional to the angular frequency. Therefore, the loss tangent decreases with frequency increase.

However, it is worth noting that the loss tangent begins to increase when the frequency is 10^4–10^5 Hz. This phenomenon is also consistent with the results of other researchers [15, 56, 57]. The dipolar relaxation

polarization of PVDF, which is related to the micro-Brownian motion of the whole chain and known as α relaxation, plays an important role in this phenomenon [58, 59]. In order to investigate the α relaxation, the following frequency-dependent electrical modulus formalism are given [6]:

$$M' = \frac{\varepsilon'}{\varepsilon'^2 + \varepsilon''^2} \tag{19}$$

$$M'' = \frac{\varepsilon''}{\varepsilon'^2 + \varepsilon''^2} \tag{20}$$

$$M^* = M' + iM'' = \frac{1}{\varepsilon^*}, \tag{21}$$

where M' and M' are the real and imaginary components of the electric modulus, respectively, ε' is the real component of the dielectric constant, ε'' is the imaginary component of the dielectric constant. Figure 6 (e and f) shows the variations of M' and M'' of all composites as a function of frequency. They are characterized by very low value of M' and M'' in the low-frequency region and an increase in the value of M' and M'' with the frequency, which may be attributed to the conduction phenomena due to the short range mobility of charge carriers and it indicates the obvious relaxation behavior in all composites [60].

In addition, the loss tangents of KNNL-Z/PVDF/ZnO composites are higher than that of KNNL-Z/PVDF composite. This is due to the space charge effects, in the other words, it means that ZnO induces more space charge and interfacial polarization among PVDF and their interfaces [21]. This is also one of the reasons why the dielectric constant is enhanced in the above analysis. Furthermore, it is also found that the relatively high conductivity may lead to an increase in loss tangent [61]. Figure 6h depicts the conductivity σ of KNNL-Z/PVDF composite and KNNL-Z/PVDF/ZnO composites at room temperature (1 kHz). With the increase of ZnO doping, the electrical conductivity of the composites increase. Interestingly, at low doping levels (2 wt%), the ZnO2 doped into composite had a higher conductivity σ than that of ZnO1 doped into composite. With the increase of ZnO addition, the electrical conductivity of the composite doped with ZnO1 was gradually higher than that of doped with ZnO2. The increase in conductivity may be due to enhancement in the mobility of electrons. Low conductivity of KNNL-Z/PVDF composite is due to the polymer chains between and ceramic particles through the grain boundaries and compactness. With the increase of the doping amount of ZnO, ZnO particles can be coupled through the grain boundaries to facilitate the movement of charge [40].

3.7 Piezoelectric properties

The piezoelectric strain coefficient (d coefficients) and piezoelectric voltage coefficient (g coefficients) are vital indicators for the application of this material in the field of sensors. They are defined by

$$d_{ij} = \frac{dP_i}{d\sigma_j} \tag{22}$$

$$g_{ij} = \frac{dE_i}{d\sigma_j} \tag{23}$$

$i = 1, 2, 3$ and $j = 1, 2, 3, 4, 5, 6$

where P_i and E_i are the polarization (vector) and electric field (vector), respectively, σ_j is the stress. The d and g coefficients are related to each other. The relationship between d and g coefficients can be described as in Eq. (24):

$$g_{ij} = \frac{d_{ij}}{k_0 k}, \tag{24}$$

where k is the dielectric constant and k_0 is the permittivity of free space. For most transducer applications, the requirement is a piezoelectric material that has high d and g values. In this work, the piezoelectric coefficients d_{33} and g_{33} are investigated.

The piezoelectric coefficients d_{33} of all samples which were placed for 24 h are as shown in Fig. 7. At the same level of ZnO loading, it is obvious that d_{33} values of KNNL-Z/PVDF/ZnO composites are higher than these of KNNL-Z/PVDF composite. For example, the d_{33} of KNNL-Z/PVDF/ZnO2 doped with 10 wt% ZnO2 can reach 55 pC/N, which is 1.5 times of the d_{33} of KNNL-Z/PVDF composite. The results indicated that ZnO nanoparticles
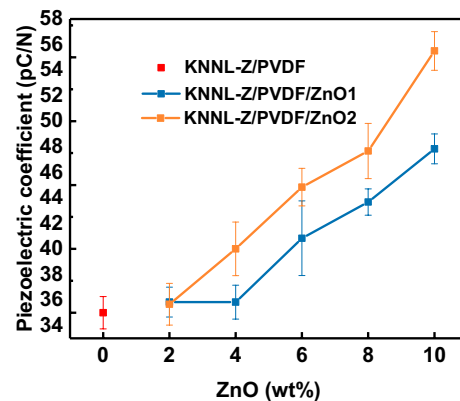
Fig. 7 The piezoelectric coefficients d_{33} of the all samples on weight content of ZnO (24 h)

can greatly improve the piezoelectric properties of the composite. According to our previous research [62], we found the addition of ZnO prepared by another method into $(0.970(0.95(K_{0.485}Na_{0.515})NbO_3\text{-}0.05LiSbO_3)\text{-}0.015CuO\text{-}0.015Al_2O_3)$/PVDF composite also significantly improved the dielectric and piezoelectric properties of the ternary composite, which seems to indicate that the use of ZnO to improve the dielectric and piezoelectric properties of the ternary composite does not impose too harsh conditions on the selection of KNN series ceramics. Hence, we think the enhancement of piezoelectric coefficients d_{33} of the composites doped by ZnO may be ascribed to three factors: (1) From the FTIR analysis, the interaction between polymer chains and ZnO nanoparticles resulted in growth of β phase. The β phase is the mostly responsible for the piezoelectric properties of PVDF. (2) The increase in dielectric constant with the increase in ZnO content promotes more dipole polarization in the composites. This high dipole polarization is responsible for the enhancement of the piezoelectric properties [63]. (3) In both studies, we noted that the addition of ZnO resulted in slight changes in cell parameters a, c, and lattice strain. In this work, the presence of lattice strain in the composite is confirmed by XRD studies (Table 1). Zhang and Chen-liang Hsu et al. found the correlation between piezoelectric properties with lattice strain [22, 64]. It may be that Zn^{2+} introduces local lattice distortion in the lattice, which destroys the local symmetry of the crystal. The electric dipole moment generated by the ion pair then provides an electric field to the nearby region, which causes the reverse displacement of the positive and negative charge of the ion pair to the nearby region, resulting in local polarization. We believe that this is the main reason that ZnO is added to the composite to improve the piezoelectric performance. Moreover, the aging characteristic of the d_{33} for all samples is shown in Table 3. It is found that the d_{33} of all samples is not changed significantly in 30 days. The result shows that the all samples have good piezoelectric stability. For another, d_{33} and g_{33} are related by

$$g_{33} = \frac{d_{33}}{\varepsilon_{33}^T}, \tag{25}$$

where ε_{33}^T is the 'free' dielectric constant. It can be calculated by Eq. (26):

$$\varepsilon_{33}^T = \frac{C^T \times L}{A}, \tag{26}$$

where C^T is the capacitance at 1 kHz, A and L are the electrode area and thickness of the sample, respectively. In some respects, $d_{33} \times g_{33}$ can represent a performance of a piezoelectric material for energy harvesting, it is expressed as the figure of merit (*FOM*) like the following equation:

$$FOM = d_{33} \times g_{33} = \frac{d_{33}^2 \times A}{C^T \times L} \tag{27}$$

Figure 8a and b shows the g_{33} and *FOM* of all composites. All composites basically showed a trend, that is, when doped with a very small amount of ZnO (less than 2 wt%), both the g_{33} and *FOM* of the composites showed a trend of decrease, while when doped with more ZnO (above 2 wt%), g_{33} and *FOM* gradually increased, basically presenting a V-shaped curve. Especially, the composite with 10 wt% ZnO2 nanocake has $g_{33}= 18.57 \times 10^{-3}$ Vm/N and *FOM* = 1.031 pm^2/N. This is very similar to the trend of *FOM* found by Yu.et al. [65]. At high concentration of ZnO (above 10 wt%), our sample has great technical advantages, and its piezoelectric voltage coefficient g_{33} and *FOM* are significantly better than these of the KNNL-Z/PVDF composite.

4 Conclusion

The $0.997(K_{0.475}Na_{0.495}Li_{0.03})$ NbO$_3$–0.003ZrO$_2$ ceramic was prepared by conventional solid-state reaction method. The PVDF polymer and ZnO1 nanoparticles were purchased from commercial companies. The ZnO2 nanoparticles were synthesized by hydrothermal method using Zn (CH$_3$COO)$_2$·2H$_2$O, CTAB, and NaOH. Subsequently, the

Table 3 The variation of d_{33} with time in all composites

Sample	KNNL-Z/PVDF	KNNL-Z/PVDF/ZnO1					KNNL-Z/PVDF/ZnO2				
ZnO (wt%)	0	2	4	6	8	10	2	4	6	8	10
Days	d_{33} (pC/N)										
5	35	34	36	39	44	49	36	39	45	48	55
10	35	36	36	39	43	49	36	40	44	45	54
15	32	36	36	39	43	50	36	40	45	46	52
20	33	36	35	39	42	49	37	40	45	46	52
25	32	35	35	39	42	49	35	39	44	46	52
30	32	36	35	39	42	49	36	37	45	46	53
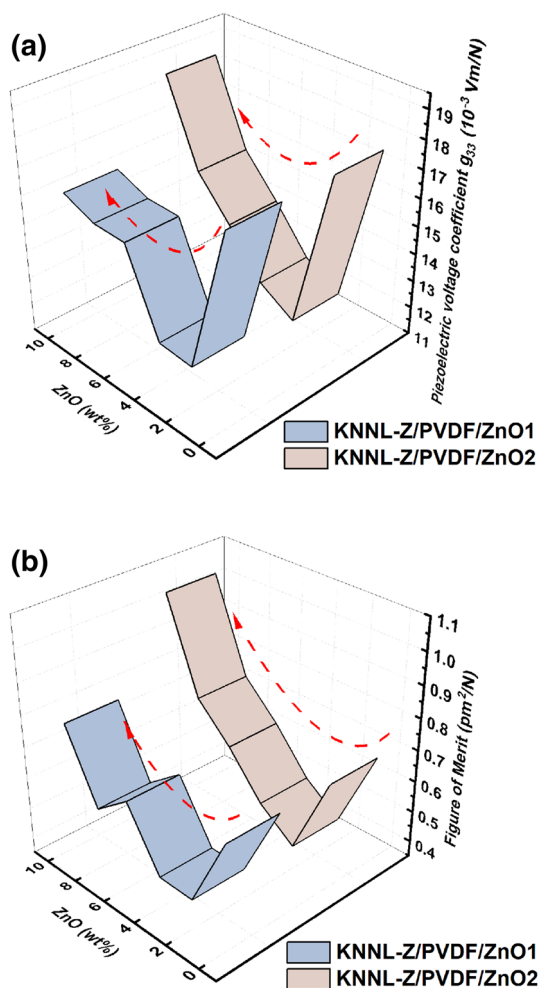
Fig. 8 The **a** g_{33} and **b** *FOM* of the composites as a function of the weight fraction of ZnO

two kinds of composites were fabricated by hot-pressing process using KNNL-Z ceramic powder, two kinds of ZnO particles, and PVDF polymer. From the X-ray studies, the ceramic is a perovskite phase with orthorhombic symmetry and without any impurity phase. The PVDF mainly possesses α, β, and γ phases and two kinds of ZnO possess hexagonal wurtzite structures. The ZnO particles can increase the relative fraction of β phase of the PVDF matrix from FTIR analysis, and from density studies, the increase in ZnO content would lead to a gradual decrease in porosity in the composite. The results show that the thermal stability, dielectric, and piezoelectric properties of the composites doped with ZnO are significantly improved compared with these of the composite without ZnO addition. Especially, when the ZnO1 content is 10 wt%, the crystallization peak temperature of KNNL-Z/PVDF/ZnO1 composite is 3 °C higher than that of KNNL-Z/PVDF composite, and the composite exhibits a dielectric permittivity as high as 469.4, which is 1.6 times higher than that of KNNL-Z/PVDF composite at

100 Hz. At the same ZnO content, the piezoelectric coefficient can reach 55 pC/N and all composites have good piezoelectric stability.

Compliance with ethical standards

Conflict of interest The authors declare that there is no conflict of interests regarding the publication of this article.

References

1. S. Murakami, D.W. Wang, A. Mostaed, A. Khesro, A. Feteira, D.C. Sinclair, Z.M. Fan, X.L. Tan, I.M. Reaney, J. Am. Ceram. Soc. **101**, 5428–5442 (2018)
2. Z.M. Dang, T. Zhou, S.H. Yao, J.K. Yuan, J.W. Zha, H.T. Song, J.Y. Li, Q. Chen, W.T. Yang, J. Bai, Adv. Mater. **21**, 2077–2082 (2009)
3. D.Q. Zhang, D.W. Wang, J. Yuan, Q.L. Zhao, Z.Y. Wang, M.S. Cao, Chin. Phys. Lett. **25**, 4410–4413 (2008)
4. L.Y. Yang, X.Y. Li, E. Allahyarov, P.L. Taylor, Q.M. Zhang, L. Zhu, Polymer **54**, 1709–1728 (2013)
5. Q.G. Chi, L. Gao, X. Wang, Y. Chen, J.F. Dong, Y. Cui, Q.Q. Lei, AIP Adv. **5**, 117103 (2015)
6. P. Thomas, S. Satapathy, K. Dwarakanath, K.B.R. Varma, Express Polym. Lett. **4**, 632–643 (2010)
7. Y. He, J.M. Hong, Adv. Mater. Process. **313**, 1818–1821 (2011)
8. Y.H. Jin, N. Xia, R.A. Gerhardt, Nano Energy **30**, 407–416 (2016)
9. P. Thakur, A. Kool, N.A. Hoque, B. Bagchi, F. Khatun, P. Biswas, D. Brahma, S. Roy, S. Banerjee, S. Das, Nano Energy **44**, 456–467 (2018)
10. L. Weng, P.H. Ju, H.X. Li, L.W. Yan, L.Z. Liu, J. Wuhan Univ. Technol. **32**, 958–962 (2017)
11. K.Y. Shin, J.S. Lee, J. Jang, Nano Energy **22**, 95–104 (2016)
12. Y. Zhang, Y. Wang, Y. Deng, M. Li, J.B. Bai, ACS Appl. Mater. Interfaces **4**, 65–68 (2012)
13. W. Wu, X.Y. Huang, S.T. Li, P.K. Jiang, T. Toshikatsu, J. Phys. Chem. C **116**, 24887–24895 (2012)
14. K. Yu, S. Hu, W.D. Yu, J.Q. Tan, J. Electron. Mater. **48**, 2329–2337 (2019)
15. A.K. Zak, W.C. Gan, W.A. Majid, M. Darroudi, T.S. Velayutham, Ceram. Int. **37**(5), 1653–1660 (2011)
16. K. Yu, H. Wang, Y.C. Zhou, Y.Y. Bai, Y.J. Niu, J. Appl. Phys. **113**, 034105 (2013)
17. T. Lusiola, A. Hussain, M.H. Kim, T. Graule, F. Clemens, Actuators **4**, 99–113 (2015)
18. Y. Huan, X.H. Wang, T. Wei, P.Y. Zhao, J. Xie, Z.F. Ye, L.T. Li, J. Eur. Ceram. Soc. **37**, 2057–2065 (2017)
19. K. Kumari, A. Prasad, K. Prasad, J. Mater. Sci. Technol. **27**, 213–217 (2011)
20. Y.C. Lee, T.K. Lee, J.H. Jan, J. Eur. Ceram. Soc. **31**, 3145–3152 (2011)
21. H. Parangusan, D. Ponnamma, M.A. AlMaadeed, RSC Adv. **7**, 50156–50165 (2017)
22. Y. Zhang, C.H. Liu, J.B. Liu, J. Xiong, J.Y. Liu, K. Zhang, Y.D. Liu, M.Z. Peng, A.F. Yu, A.H. Zhang, Y. Zhang, Z.W. Wang, J.Y. Zhai, Z.L. Wang, ACS Appl. Mater. Interfaces **8**, 1381–1387 (2016)

23. K. Yu, S. Hu, W.D. Yu, J.Q. Tan, J. Electron. Mater. **48**, 5919–5932 (2019)
24. V.V. Atuchin, C.C. Ziling, D.P. Shipilova, N.F. Beizel, Ferroelectrics **100**, 261–269 (1989)
25. A. Watcharapasorn, S. Jiansirisomboon, Ceram. Int. **34**, 769–772 (2008)
26. C.J. Dias, D.K. DasGupta, IEEE Trans. Dielect. Electr. Insul. **3**, 706–734 (1996)
27. I.Y. Abdullah, M. Yahaya, M.H.H. Jumali, H.M. Shanshool, Opt. Quant. Electron. **48**, 149 (2016)
28. T. Greeshma, R. Balaji, S. Jayakumar, Ferroelectrics Lett. **40**, 41–55 (2013)
29. L. Yu, P. Cebe, Polymer **50**, 2133–2141 (2009)
30. S.K. Ghosh, M.M. Alam, D. Mandal, RSC Adv. **4**, 41886–41894 (2014)
31. A.C. Lopes, S.A. Carabineiro, M.F. Pereira, G. Botelho, S. Lanceros-Mendez, ChemPhysChem **14**, 1926–1933 (2013)
32. P. Martins, C. Caparros, R. Goncalves, P.M. Martins, M. Benelmekki, G. Botelho, S. Lanceros-Mendez, J. Phys. Chem. C **116**, 15790–15794 (2012)
33. V.V. Atuchin, A.S. Aleksandrovsky, O.D. Chimitova, T.A. Gavrilova, A.S. Krylov, M.S. Molokeev, A.S. Oreshonkov, B.G. Bazarov, J.G. Bazarova, J. Phys. Chem. C **118**, 15404–15411 (2014)
34. K.A. Kokh, V.V. Atuchin, T.A. Gavrilova, N.V. Kuratieva, N.V. Pervukhina, N.V. Surovtsev, Solid State Commun. **177**, 16–19 (2014)
35. J.B. Zhong, J.Z. Li, Z.H. Xiao, W. Hu, X.B. Zhou, X.W. Zheng, Mater. Lett. **91**, 301–303 (2013)
36. H.M. Moghaddam, H. Malkeshi, J. Mater. Sci. **27**, 8807–8815 (2016)
37. X.M. Sun, X. Chen, Z.X. Deng, Y.D. Li, Mater. Chem. Phys. **78**, 99–104 (2003)
38. J. Li, C.M. Zhao, K. Xia, X. Liu, D. Li, J. Han, Appl. Surf. Sci. **463**, 626–634 (2019)
39. A.P. Indolia, M.S. Gaur, J. Therm. Anal. Calorim. **113**, 821–830 (2013)
40. A. Batool, F. Kanwal, M. Imran, T. Jamil, S.A. Siddiqi, Synth. Met. **161**, 2753–2758 (2012)
41. L.J. Fang, W. Wu, X.Y. Huang, J.L. He, P.K. Jiang, Compos. Sci. Technol. **107**, 67–74 (2015)
42. W. Gao, B. Zhou, Y.H. Liu, X.Y. Ma, Y. Liu, Z.C. Wang, Y.C. Zhu, Polym. Int. **62**, 432–438 (2013)
43. A. Lonjon, L. Laffont, P. Demont, E. Dantras, C. Lacabanne, J. Phys. D **43**, 345401 (2010)
44. A.S. Bhatt, D.K. Bhat, M.S. Santosh, J. Appl. Polym. Sci. **119**, 968–972 (2011)
45. Z.M. He, J. Ma, R.F. Zhang, T. Li, J. Eur. Ceram. Soc. **23**, 1943–1947 (2003)
46. E. Atamanik, V. Thangadurai, J. Phys. Chem. C **113**, 4648–4653 (2009)
47. A. Ashok, T. Somaiah, D. Ravinder, C. Venkateshwarlu, C.S. Reddy, K.N. Rao, M. Prasad, World J. Condens. Matter Phys. **2**, 257–266 (2012)
48. Y. Chen, S.X. Xie, H.M. Wang, Q. Chen, Q.Y. Wang, J.G. Zhu, Z.W. Guan, J. Alloy. Compd. **696**, 746–753 (2017)
49. Y. Zhou, J.C. Zhang, L. Li, Y.L. Su, J.R. Cheng, S.X. Cao, J. Alloy. Compd. **484**, 535–539 (2009)
50. K.T. Selvi, K. Alamelumangai, M. Priya, M. Rathnakumari, P.S. Kumar, S. Sagadevan, J. Mater. Sci. **27**, 6457–6463 (2016)
51. W.Y. Zhou, Z.J. Wang, L.N. Dong, X.Z. Sui, Q.G. Chen, Compos. Part A **79**, 183–191 (2015)
52. J.H. Choi, J.S. Seo, S.N. Cha, H.J. Kim, S.M. Kim, Y.J. Park, S.W. Kim, J.B. Yoo, J.M. Kim, Jpn. J. Appl. Phys. **50**, 1 (2011)
53. O.J. Cheong, J.S. Lee, J.H. Kim, J. Jang, Small **12**, 2567–2574 (2016)
54. S.T. Wang, J. Sun, L. Tong, Y.M. Guo, H. Wang, C.C. Wang, Mater. Lett. **211**, 114–117 (2018)
55. I.S. Elashmawi, E.M. Abdelrazek, H.M. Ragab, N.A. Hakeem, Phys. B **405**, 94–98 (2010)
56. S. Adireddy, V.S. Puli, T.J. Lou, R. Elupula, S.C. Sklare, B.C. Riggs, D.B. Chrisey, J. Sol-Gel Sci. Technol. **73**, 641–646 (2015)
57. S.H. Liu, J.W. Zhai, RSC Adv. **4**, 40973–40979 (2014)
58. Z. Wang, T. Wang, C. Wang, Y.J. Xiao, P.P. Jing, Y.F. Cui, Y.P. Pu, ACS Appl. Mater. Interfaces **9**, 29130–29139 (2017)
59. B.C. Luo, X.H. Wang, Y.P. Wang, L.T. Li, J. Mater. Chem. A **2**, 510–519 (2014)
60. J.G.L. Peng, J.T. Zeng, L.Y. Zheng, G.R. Li, N. Yaacoub, M. Tabellout, A. Gibaud, A. Kassiba, J. Alloy. Compd. **796**, 221–228 (2019)
61. Q.Q. Zhang, F. Gao, G.X. Hu, C.C. Zhang, M. Wang, M.J. Qin, L. Wang, Compos. Sci. Technol. **118**, 94–100 (2015)
62. K. Yu, S. Hu, W.D. Yu, J.Q. Tan, Opt. Quant. Electron. **51**, 336 (2019)
63. S. Paria, S.K. Karan, R. Bera, A.K. Das, A. Maitra, B.B. Khatua, Ind. Eng. Chem. Res. **55**, 10671–10680 (2016)
64. C.L. Hsu, I.L. Su, T.J. Hsueh, RSC Adv. **5**, 34019–34026 (2015)
65. X.L. Yu, Y.D. Hou, M.P. Zheng, J. Yan, W.X. Jia, M.K. Zhu, J. Am. Ceram. Soc. **102**, 275–284 (2019)